

Single Image Rolling Shutter Removal with Diffusion Models

Zhanglei Yang, Haipeng Li, *Student Member, IEEE*, Mingbo Hong, Jiajun Li, Bing Zeng, *Fellow, IEEE*, Shuaicheng Liu, *Senior Member, IEEE*

Abstract—We present RS-Diffusion, the first Diffusion Models-based method for single-frame Rolling Shutter (RS) correction. RS artifacts compromise visual quality of frames due to the row-wise exposure of CMOS sensors. Most previous methods have focused on multi-frame approaches, using temporal information from consecutive frames for the motion rectification. However, few approaches address the more challenging but important single frame RS correction. In this work, we present an “image-to-motion” framework via diffusion techniques, with a designed patch-attention module. In addition, we present the RS-Real dataset, comprised of captured RS frames alongside their corresponding Global Shutter (GS) ground-truth pairs. The GS frames are corrected from the RS ones, guided by the corresponding Inertial Measurement Unit (IMU) gyroscope data acquired during capture. Experiments show that our RS-Diffusion surpasses previous single RS correction methods. Our method and proposed RS-Real dataset lay a solid foundation for advancing the field of RS correction.

Index Terms—Diffusion models, homography, gyroscope, transformer.

I. INTRODUCTION

Rolling shutter (RS) is a common effect encountered when capturing images with CMOS sensors. It results from varying exposure times for different rows in each frame, causing artifacts like distorted straight lines and skewed image content, as shown in Fig. 1 (Rolling-Shutter Image). These distortions are not only visually unpleasing but also detrimental to downstream tasks [1]–[5]. Prior methods for RS removal can be categorized as multi-frame and single-frame based. The former relies on temporal motion in consecutive frames for motion compensation, while the latter solely depends on a single frame for restoration. Single-frame RS correction is particularly challenging yet crucial in data-scarce situations. Many existing methods, including non-learning-based approaches [6]–[10], rely on salient structures, such as straight lines. However, they may falter in cases where such salient structures are absent.

The majority of deep RS correction methods are multi-frame based [11]–[15], with only a few considering a single

frame as input. Among single-frame methods, Rengarajan *et al.* [7] directly learn the mapping between global shutter (GS) and RS frames, facing the challenge of large solution space for row-wise motion estimation. Zhuang *et al.* [9] addressed this by estimating an additional depth map, although depth estimation from RS frames is inherently ill-posed. Recently, Yan *et al.* [16] introduced a deep homography mixture model, achieving the current best performance by embedding motion in a subspace and learning coefficients to combine pre-learned motion flow bases.

Recent advancements in generative models [17]–[19], including Diffusion Models (DMs) [20], [21], have significantly advanced the field of Artificial Intelligence. Notably, DMs excel in performing various motion-related tasks, notably in human motion generation [22] and in estimating depth/optical flow [23]. Meanwhile, DMs have shown strength in solving ill-posed problems, such as image restoration [24]–[27], where inferring accurate solutions from ambiguous data is difficult. Therefore, drawing on these insights and inspirations, in this work, we introduce a novel single-frame RS correction method based on DMs, namely **RS-Diffusion**. DMs are adept at generating data from Gaussian distributions through multiple sampling steps and can be conditioned on additional information, such as text or images. Leveraging the transformative capabilities of DMs, we are capable of correcting RS images to GS images. Our framework, built on CFG [28] and DDIM [29], uses a downsampled RS image I_{RS} as a conditioning element, concatenated with Gaussian noise. This input is processed by DMs in very few steps to produce a motion field G , which is then applied to remap I_{RS} to eliminate RS artifacts. Additionally, we introduce a patch-attention module based on prior RS motion patterns to enhance results. We visualize the produced correcting field and our corrected result in the first row of Fig. 1.

On the other hand, high-quality datasets play a crucial role. To meet the demand, we adhere to two essential criteria [30]: the *label criterion*, which requires precise alignment of RS correction motion as ground-truth labels between RS-GS pairs, and the *realism criterion*, which ensures that both the image content and RS motion remain realistic. However, existing RS datasets often fall short of meeting these criteria. The synthesized dataset can provide accurate labels, but violates realism criterion. In contrast, the captured images can suffice the realism, but the label is not accurate. For example, capturing with two cameras, one RS and one GS, suffers from parallax between two cameras.

To resolve these issues, we introduce Intra Gyro Field

Manuscript submitted on May 27, 2024. This work was supported in part by the National Natural Science Foundation of China (NSFC) under Grant Nos. 62372091, 61872405 and in part by Sichuan Science and Technology Program of China under grant No.2023NSFSC0462.

Zhanglei Yang, Haipeng Li, Bing Zeng and Shuaicheng Liu are with School of Information and Communication Engineering, University of Electronic Science and Technology of China, Chengdu, Sichuan, China; Mingbo Hong is with Megvii Research Chengdu, Sichuan, China; Jiajun Li is with noumena.ai, Beijing, China.

Zhanglei Yang and Haipeng Li have contributed equally; Corresponding author: Shuaicheng Liu (liushuaicheng@uestc.edu.cn)

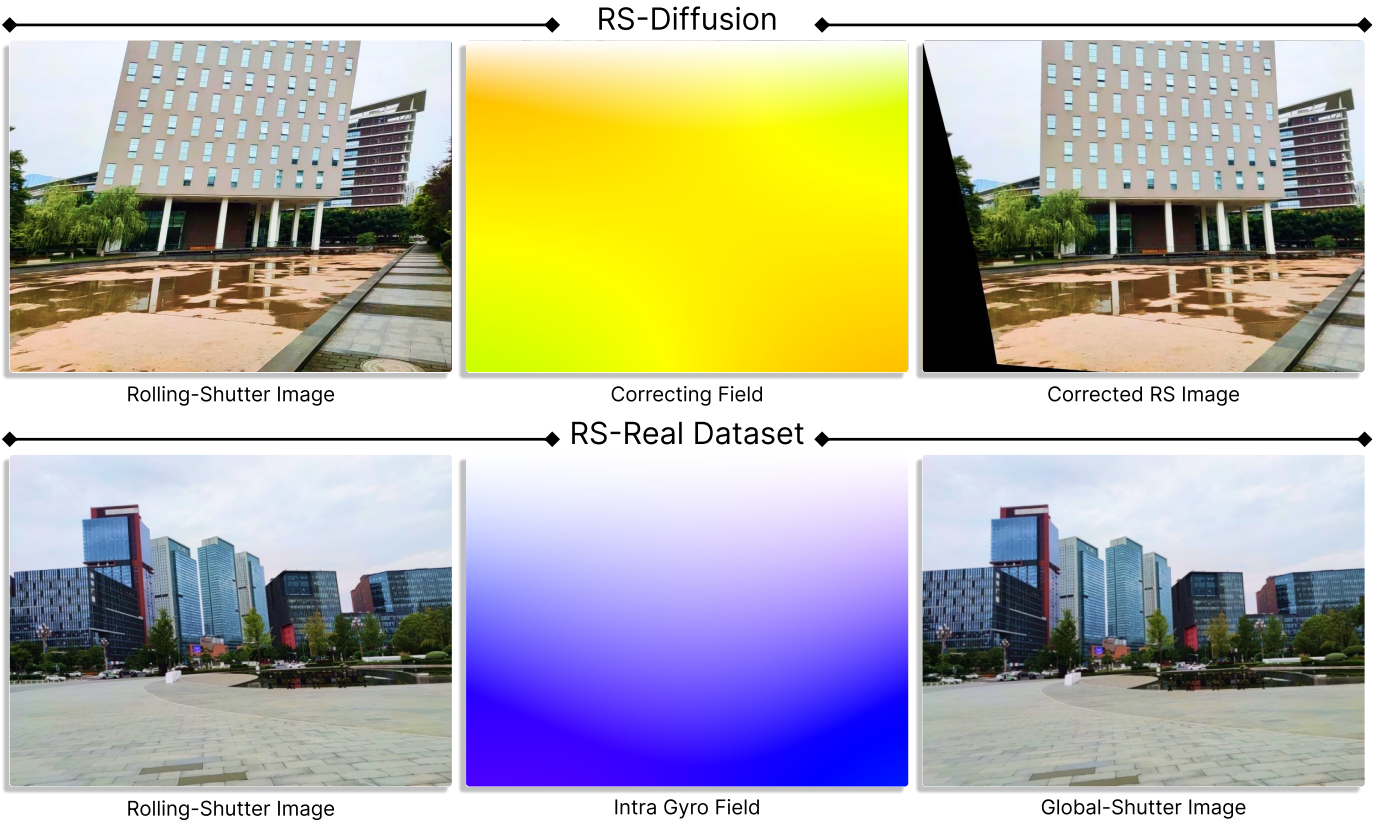


Fig. 1. Illustration of our results and the proposed dataset: the first row demonstrates that for a rolling-shutter (RS) image, our proposed RS-Diffusion framework produces a correcting field (in the optical flow visualization, different colors represent different directions and intensities of motion) leading to the corresponding corrected RS image. The second row illustrates our proposed RS-Real dataset, which includes, from left to right, a different RS image taken in real-world scenes, the ground-truth correcting field named Intra Gyro Field (IGF), which is used to correct the RS image to a global-shutter (GS) image, and the corresponding ground-truth GS image.

(IGF) pipeline, leveraging Inertial Measurement Unit (IMU) gyroscope sensors to record camera rotations during capture. Specifically, we firstly achieve accurate frame-gyro data synchronization. Next, these rotations are translated into a series of homography matrices, further converted into motion fields as RS correction ground-truth (GT) labels. With the help of IGF, we create the **RS-Real** dataset, which, for the first time, satisfies both the label and realism criteria in RS correction. The dataset contains 44,000 train and 1,000 test samples. A case is shown in Fig. 1, where the second row shows a captured RS image, the IGF between RS-GS pair and its GS image.

In summary, our diffusion model-based framework advances the state-of-the-art in single-image RS correction, while could run inference in real-time speed, i.e., up to 28.1 ms per frame on one NVIDIA 2080Ti. The RS-Real dataset, containing high-quality training pairs, addresses the scarcity of qualified datasets in the RS task. Our contributions include:

- We propose the first diffusion-based framework for single image rolling shutter removal, namely **RS-Diffusion**.
- We introduce a pipeline for correcting RS images with recorded IMU gyro readings, which delivers accurate rectified RS images as ground-truth labels for training and testing, yielding the first real RS dataset, **RS-Real**.
- Experiments show that our approach achieves state-of-the-art performance on public benchmarks, exhibiting both generalizability and applicability.

II. RELATED WORK

A. Rolling Shutter Correction Methods.

Multi-frame rectification methods use spatial-temporal information, with investigations into per-pixel motion vectors [11], image feature tracking [12], and affine models [31], now enhanced by 3D data [13]. Advances in deep learning include pixel-wise velocity estimation [32], the use of optical flow for deep feature warping [33], adaptive warping techniques [34], transformer-based one-stage networks [35], and studies on bilateral motion fields [36], with recent work focusing on RS removal and deblurring [37]. Additionally, some studies explore the restoration of GS images by leveraging dual-RS cameras [38] and then achieve temporal super-resolution [39] via a self-supervised learning strategy [40]. Classical single-image methods mostly utilize salient lines for RS correction [6], [41]. Deep learning for single RS image correction is less common but includes neural networks trained on paired images [7], employing motion models and depth map estimations [9]. A novel deep homography mixture model shows state-of-the-art results [16]. We introduce diffusion models (DMs) for single RS rectification, demonstrating their effectiveness and generalizability in motion extraction.

B. Diffusion Models.

Diffusion models (DMs), based on stochastic diffusion processes [42], efficiently transform data distributions through

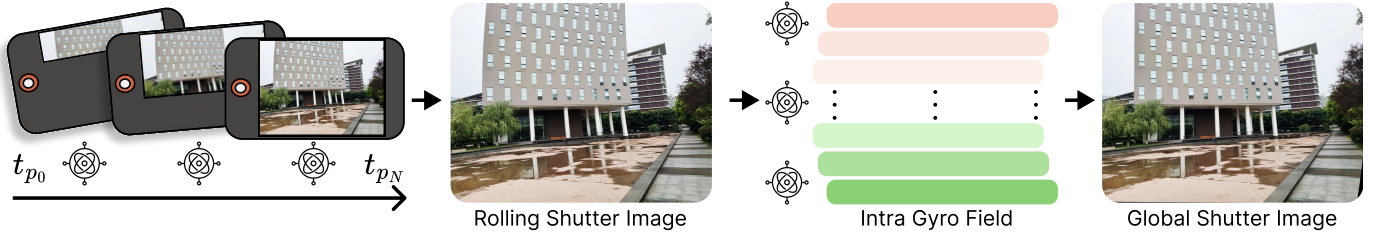


Fig. 2. Rolling shutter image \mathbf{I}_{RS} , is introduced by high-frequency shake with a row-wise exposure CMOS camera. The gyroscope can accurately record these motions, which are then transformed into a motion field, $\mathbf{G} \in \mathbf{R}^{2 \times H \times W}$. This field is referred to as the Intra Gyro Field (IGF). With \mathbf{G} , we are able to correct \mathbf{I}_{RS} , resulting in a Global Shutter Image, \mathbf{I}_{GS} .

Gaussian transitions and iterative denoising using the data distribution gradient [43]. DDPM [20] employs discrete steps in this process, and Song *et al.* [21] further refines the methodology via stochastic differential equations (SDE). DDIM [29] accelerates reverse sampling through subsequence sampling and ordinary differential equations (ODEs). Conditioned data generation progresses with classifier-based [44], [45] and classifier-free (CFG) techniques [28], including cross-attention-based integration [46] and distinguishing between range-null space for conditioned generation [47]. DMs also contribute to motion-centric tasks, from video generation [48], image rectangling [49], hand mesh rendering [50] and homography rendering/estimation [51], optical flow [23] to human motion [22]. Our work extends DMs to the domain of rolling shutter removal.

C. Gyroscope-based Motion Methods

Gyroscopes are pivotal for diverse applications such as video stabilization [52], [53], deblurring [54], [55], optical image stabilization (OIS) [56], simultaneous localization and mapping [57], ego-motion [58], [59], and human pose and motion estimation [60], [61], with growing using in RS correction if gyroscope data is accessible during the capturing [62]. In this work, instead of directly using online captured gyroscope data to promote the performances of different applications. We use the gyroscope data to create a dataset. Our work utilizes gyroscope synchronization at the Android HAL for precise calibration [59], [63], enabling the creation of a **RS-Real** dataset for rolling shutter effect research, incorporating authentic RS pairings for enhanced training and validation. Note that, our method does not need gyro readings during the model inference.

III. METHOD

A. Overview

We present a pipeline named Intra Gyro Field (IGF) designed to create a realistic and precisely annotated dataset through combined engineering and algorithmic efforts, as discussed in Sec. III-B. Furthermore, we propose a novel and general framework based on diffusion models, incorporating a specialized patch attention (PA) module, which is aimed at correcting rolling shutter (RS) images to global shutter (GS) quality, as described in Sec. III-C.

B. Intra Gyro Field

Gyroscope records the relative camera 3D rotation in a relative time and it is possible to convert the gyroscope readings into a 2D motion field to achieve alignment between two consecutive frames [64]. In this chapter, we demonstrate how to leverage the gyroscope to correct RS effect for a single image and thus propose an Intra Gyro Field (IGF). Specifically, given the 3-axis angular velocity readings (row \mathbf{v}_r , pitch \mathbf{v}_p and yaw \mathbf{v}_y) and relative time intervals Δt between gyro readings. The 3-axis angular angles ($\angle r, \angle p, \angle y$) can be computed as:

$$\angle r = \mathbf{v}_r \cdot \Delta t, \quad \angle p = \mathbf{v}_p \cdot \Delta t, \quad \angle y = \mathbf{v}_y \cdot \Delta t. \quad (1)$$

Then we utilize the Rodrigues Formula [65] to convert rotation angles into the rotation matrix $\mathbf{R}(\Delta t) \in SO(3)$. In order to bridge the relationship between 3D camera pose and 2D image motion, we choose to use the homography matrix \mathbf{H} . The homography matrix represents the relationship between two different perspectives of the same scene, more specifically, the conditions for its validity are satisfied when the camera motion is purely rotational or when the contents lie in the same plane [66]. Theoretically, given 3D rotation matrix $\mathbf{R}(\Delta t)$ and translation vector $\mathbf{t}(\Delta t)$, we can represent \mathbf{H} as:

$$\mathbf{H} = \mathbf{K} \left(\mathbf{R}(\Delta t) + \mathbf{t}(\Delta t) \frac{\mathbf{n}^T}{d} \right) \mathbf{K}^{-1}, \quad (2)$$

where \mathbf{n}^T represents the normal vector of a certain plane, d is the distance between the camera center and the plane, and \mathbf{K} is the camera intrinsic matrix.

In this work, we do not incorporate translations and only use gyroscope data to model the homography matrix, the reasons are threefold. Firstly, the rolling shutter effect caused by camera shake occurs primarily due to rotational movements [52]. Secondly, even though translations can be gathered from accelerometer data, they are significantly less accurate than rotational measurements [67], [68]. Lastly, according to Eq. 2, we can find that translation is correlated to depth, but accurately estimating depth maps can be another non-trivial problem. As a result, we can formulate a rotational-only homography:

$$\mathbf{H} = \mathbf{K} (\mathbf{R}(\Delta t)) \mathbf{K}^{-1}. \quad (3)$$

The gyroscope records N readings during the capture of one image, it thus can record and produce N camera rotation



Fig. 3. **RS-Real** dataset contains data pairs featuring various RS motion patterns and different intensities, all of which are captured in diverse scenes.

matrices $(\mathbf{R}_1(\Delta t), \mathbf{R}_2(\Delta t), \dots, \mathbf{R}_N(\Delta t))$. If we split the image from top to bottom into N patches $(\mathbf{p}_1, \mathbf{p}_2, \dots, \mathbf{p}_N)$, these rotation matrices correspond to the motion between the first row and bottom row of patches as illustrated in Fig. 2. Moreover, the inter-patch motion is approximately to be smooth [56], [69], so we can apply the spherical linear interpolation (SLERP) to interpolate the motion to avoid the discontinuities across row patches. Subsequently, we follow Eq. 3 to produce N homography matrices $(\mathbf{H}_1, \mathbf{H}_2, \dots, \mathbf{H}_N)$ to model the 2D relationship between patches. To this end, we follow previous method [70] to convert the array of homography matrix into a motion field, it is achieved by transforming grid points by their corresponding homography and subtracting them. Lastly, this motion field is IGF, denoted as $\mathbf{G} \in \mathbf{R}^{2 \times H \times W}$, which is capable of correcting the RS effect within an image:

$$\mathbf{I}_{GS} = \text{Remap}(\mathbf{I}_{RS}, \mathbf{G}). \quad (4)$$

Dataset Collecting. Our proposed IGF effectively addresses the challenges found in previous datasets, such as unrealistic data distributions and spatio-temporal synchronization issues. By recording the RS effect with a gyroscope and subsequently recovering from it, our approach circumvents synchronization challenges by using only one camera at a time. As a result, we can flexibly capture a diverse range of realistic scenes, spanning various indoor and outdoor environments, and subjecting the camera to multiple motion patterns and speeds. This method enables us to gather a comprehensive dataset of realistic RS images, denoted as $\mathbf{X}_{RS} = \{\mathbf{I}_{RS}^0, \mathbf{I}_{RS}^1, \dots, \mathbf{I}_{RS}^k\}$, along with their correspond-

ing IGFs, $\mathbf{X}_{IGF} = \{\mathbf{G}^0, \mathbf{G}^1, \dots, \mathbf{G}^k\}$. After applying RS removal using Eq. 4, we obtain the set of GS images, $\mathbf{X}_{GS} = \{\mathbf{I}_{GS}^0, \mathbf{I}_{GS}^1, \dots, \mathbf{I}_{GS}^k\}$. We refer to this novel dataset as **RS-Real**. Examples from the dataset are illustrated in Fig. 3.

C. Diffusion Models

To correct distortions resulting from the RS effect in general cases, we utilize diffusion models adept at managing the distributional transformations of images captured under both rolling shutter (RS) and global shutter (GS) conditions.

Specifically, we leverage the diffusion models as proposed by Sohl-Dickstein *et al.* [42] and Ho *et al.* [20], which define a Markov chain process over T steps to incrementally introduce Gaussian noise into the original data distribution $\mathbf{x}_0 \sim q(\mathbf{x})$. This stepwise infusion of noise generates a sequence of increasingly distorted states $\mathbf{x}_1, \dots, \mathbf{x}_T$, defined as forward diffusion, and is mathematically represented as:

$$q(\mathbf{x}_{1:T} | \mathbf{x}_0) = \prod_{t=1}^T q(\mathbf{x}_t | \mathbf{x}_{t-1}). \quad (5)$$

Following this, a denoising model, denoted as θ , is then trained to reverse the diffusion process $p_\theta(\mathbf{x}_{t-1} | \mathbf{x}_t)$ to construct desired data samples from isotropic Gaussian noise $\mathbf{x}_T \sim \mathcal{N}(\mathbf{0}, \mathbf{I})$:

$$p_\theta(\mathbf{x}_{0:T}) = p(\mathbf{x}_T) \prod_{t=1}^T p_\theta(\mathbf{x}_{t-1} | \mathbf{x}_t). \quad (6)$$

This inversion transforms the signal from the noise-dominant Gaussian distribution back into the target data distribution. To

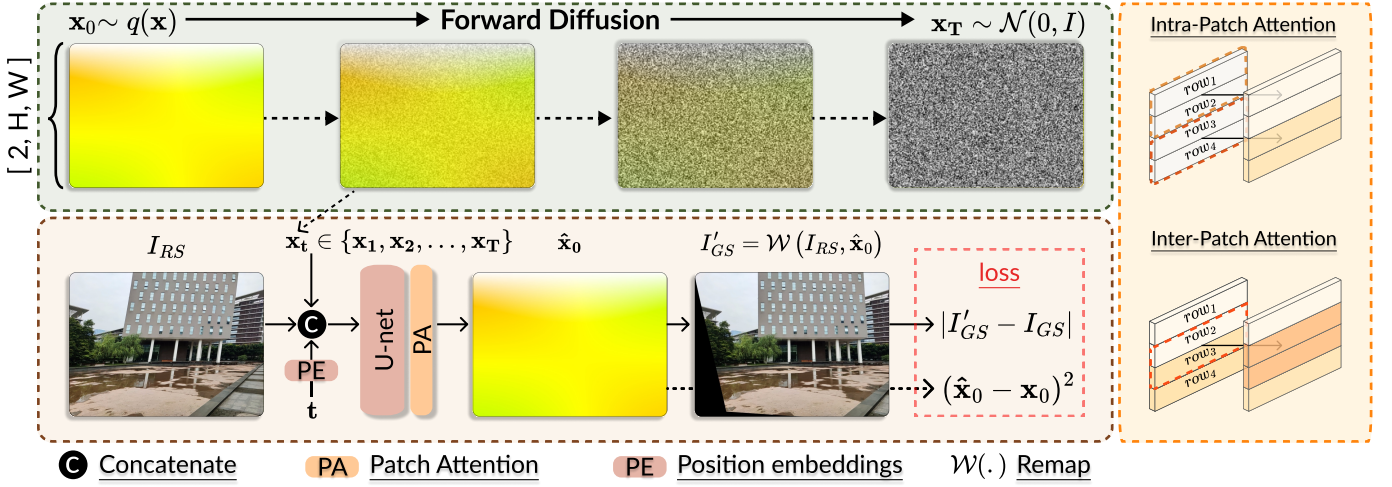


Fig. 4. Illustration of the framework: During training, \mathbf{x}_0 undergoes forward diffusion to become \mathbf{x}_t . The network θ processes the concatenated input. The Patch-Attention module, which includes both Intra-Patch and Inter-Patch attention mechanisms, enhances the relationships between patches. The resulting output, $\hat{\mathbf{x}}_0$, can be used to correct I_{RS} . The loss function comprises the MSE Loss, calculated between $\hat{\mathbf{x}}_0$ and \mathbf{x}_0 , and the photometric loss, computed between the GT GS image and I'_{GS} .

refine this reconstruction process and improve the quality of the generated samples, we can integrate conditional variables \mathbf{y} into the model as described by CFG [28]. These conditions are merged with the noisy data transitions in the model:

$$p_{\theta}(\mathbf{x}_{t-1} | \mathbf{x}_t, \mathbf{y}) = \mathcal{N}(\mathbf{x}_{t-1}; \boldsymbol{\mu}_{\theta}(\mathbf{x}_t, t, \mathbf{y}), \sigma_t^2 \mathbf{I}). \quad (7)$$

By incorporating supplementary conditions, we are able to exert enhanced control over the sample generation phase, which results in an improvement in the fidelity of the final reconstructions.

D. Rolling Shutter Removal Module

Our framework is built upon CFG [28] and DDIM [29]. We illustrate the pipeline in Fig. 4, we designate IGFs as the initial data distribution, \mathbf{x}_0 , and the RS images I_{RS} as conditions \mathbf{y} . This configuration endows the model with an “image-to-motion” capability. During the training process, \mathbf{x}_0 is noised via forward diffusion to \mathbf{x}_t , then we concatenate the I_{RS} , \mathbf{x}_t and time embedding to feed into the U-net network θ . It is imperative to note that this concatenation is introduced at various layers within the network. Finally, the output of θ is processed through the Patch-Attention module, resulting in the generated outputs $\hat{\mathbf{x}}_0$.

Patch-Attention Module. As described in previous sections, we observe that the motion patterns in RS images are consistently correlated between rows. In practice, rows are often regrouped into patches to mitigate the effects of RS. Capitalizing on this a priori, we propose an attention block to foster the inter-relationships between these patches. Our attention block operates in two stages: Firstly, the intra-patch attention phase involves evenly splitting the input into non-overlapping patches. As exemplified on the right side of Fig. 4, the feature is divided into patches (4 rows into 2 patches in this example). Within each patch, self-attention is employed to process features internally. Subsequently, the inter-patch attention stage is applied. In this phase, self-attention mechanisms are utilized

to facilitate the exchange of information between consecutive rows across different patches. This approach ensures that the relationship between adjacent patches is effectively enhanced. **Loss Function.** After computing $\hat{\mathbf{x}}_0$, we first apply the mean squared error (MSE Loss) as follows:

$$\ell_{mse} = (\hat{\mathbf{x}}_0 - \mathbf{x}_0)^2. \quad (8)$$

In addition to the MSE Loss, which facilitates learning the distribution transformation from RS images to their respective IGF, we further propose to constrain the network with an extra conditional loss. Specifically, we warp the original RS images I_{RS} via the computed IGF $\hat{\mathbf{x}}_0$ to produce corrected RS images I'_{GS} :

$$I'_{GS} = \mathcal{W}(I_{RS}, \hat{\mathbf{x}}_0), \quad (9)$$

where $\mathcal{W}(\cdot)$ represents the remapping operation. Then we calculate the photometric loss between I'_{GS} and I_{GS} :

$$\ell_{pl} = |I'_{GS} - I_{GS}|. \quad (10)$$

Consequently, the overall loss can be computed as a dynamically weighted sum. In other words, it continually adjusts ℓ_{pl} to be equal to ℓ_{mse} , formulated as:

$$\ell_{overall} = \ell_{mse} + \frac{|\ell_{mse}|}{|\ell_{pl}|} \cdot \ell_{pl}. \quad (11)$$

IV. EXPERIMENT

This section is organized as follows: We begin by the implementation details in Section IV-A and outlining both existing and our proposed datasets in Section IV-B. We then compare our method’s performance against other approaches on various benchmarks in Section IV-C, with qualitative evaluations presented in Section IV-D. The performance of our model with global shutter images as input was evaluated in Section IV-E. The generalizability of our approach is examined through experiments across different devices in Section IV-F. An in-depth analysis of our framework’s intricate design features is provided in Section IV-G.

TABLE I

COMPARISON OF PSNR, SSIM, AND EPE BETWEEN OUR METHOD AND EXISTING ONES ON **BUILDING** DATASET. THE VALUES ENCLOSED WITHIN PARENTHESES INDICATE THE STANDARD DEVIATION OF OUR RESULTS OVER 10 INFERENCE ITERATIONS.

Method	PSNR(dB) \uparrow	SSIM \uparrow	EPE \downarrow
Rengarajan <i>et al.</i> [6]	29.82	0.67	11.89
Purkait <i>et al.</i> [8]	29.22	0.55	8.32
Grundmann <i>et al.</i> [74]	32.57	0.72	3.34
Rengarajan <i>et al.</i> [7]	32.25	0.70	3.76
Kandula <i>et al.</i> [10]	32.85	0.73	2.84
Yan <i>et al.</i> [16]	33.34	0.75	1.25
RS-Diffusion	34.92 (± 0.045)	0.79 (± 0.002)	0.90 (± 0.018)

A. Implementation Details

Our model is implemented in PyTorch and trained on 8 NVIDIA 2080Ti GPUs. During the training phase, we utilized the Adam optimizer with a learning rate of 3×10^{-4} and a batch size of 64. The backbone diffusion model settings include an input resolution of 64×64 , 1,000 diffusion steps, a linear noise scheduler, and the target of predicting “ x_0 ” as the generating object. The entire training process comprised 150,000 steps and took approximately 40 hours. In the forward diffusion process, we performed 8 sampling steps with $\eta = 0$. The inference time can be up to 28.1 ms per frame on a single NVIDIA 2080Ti.

B. Dataset

In our experiments, we validate the proposed RS correction method on 3 datasets, including one long-standing public datasets and two new ones for comprehensive evaluation. To ascertain the reliability of our approach, we synchronize our evaluations with established RS image correction techniques [7], [10], [16], utilizing the **Building** dataset [71]–[73] as a standard benchmark. Additionally, we extend our test scope with a challenging dataset **RS-Homo** from Yan *et al.* [16], crafted to simulate adverse conditions like low lighting and scant textures, critical for testing diffusion model robustness. A notable contribution of this paper is the **RS-Real** dataset, detailed in Section III-B, which exploits sensor information during image capture to address common synchronization challenges and offers a new methodology for data gathering in RS scenarios.

C. Quantitative Comparison

In our study, we evaluate our RS image correction method using key metrics for visual quality and motion accuracy. Visual comparisons are done via the Peak Signal-to-Noise Ratio (PSNR) and the Structural Similarity Index Measure (SSIM) against GT GS images. The motion-based assessment considers the Endpoint Error (EPE) for correction flow accuracy. Pixels on black edges, lacking information, are omitted from our analysis. Notably, diffusion models can produce different results with each inference. Therefore, we report both the mean and the standard deviation of the results over 10 inference iterations.

TABLE II

COMPARISON OF PSNR, SSIM, AND EPE BETWEEN OUR METHOD AND YAN *et al.* [16] ON THE **RS-HOMO** DATASET. THE VALUES ENCLOSED WITHIN PARENTHESES INDICATE THE STANDARD DEVIATION OF OUR RESULTS OVER 10 INFERENCE ITERATIONS.

Method	PSNR(dB) \uparrow	SSIM \uparrow	EPE \downarrow
Yan <i>et al.</i> [16]	26.15	0.77	4.10
RS-Diffusion	36.66 (± 0.092)	0.94 (± 0.002)	1.02 (± 0.083)

TABLE III

COMPARISON OF PSNR, SSIM, AND EPE BETWEEN OUR METHOD AND YAN *et al.* [16] ON THE **RS-REAL** DATASET. THE VALUES ENCLOSED WITHIN PARENTHESES INDICATE THE STANDARD DEVIATION OF OUR RESULTS OVER 10 INFERENCE ITERATIONS.

Method	PSNR(dB) \uparrow	SSIM \uparrow	EPE \downarrow
Yan <i>et al.</i> [16]	18.48	0.55	4.18
RS-Diffusion	22.02 (± 0.031)	0.70 (± 0.001)	2.12 (± 0.010)

Building dataset. Our study compares with traditional and deep learning-based RS correction methods, as shown in Table I. Approaches using curve detection [6], [8] to discern motion patterns struggle in low-structure environments, showing subpar PSNR and SSIM, alongside elevated EPE. The homography mixtures method [74] fares better with its video sequence foundation and refined feature correspondences. However, learning methods [7], [10] have proven robust to strong outliers and complex camera motions. Yan *et al.* model [16], merging homography mixtures with learning, showcases significant strides in metric performance due to constrained motion spaces from learned bases. Our proposed technique outperforms existing methods, setting a new state-of-the-art (SOTA) across evaluated metrics and emphasizing its effectiveness.

RS-Homo dataset. The results in Table II show our diffusion models-based framework substantially improves upon Yan *et al.*’s state-of-the-art single-image model. Demonstrating great proficiency in managing challenging scenarios, our proposed method surpasses specifically designed architectures, enhancing the capability of diffusion models to address rolling shutter (RS) effects effectively.

RS-Real dataset. Our dataset, designed for realism in content, RS-motion, and label accuracy, comprises 44,000 training and 1,000 test pairs across diverse scenes. It includes RS and GS images along with GT flow. We benchmark against Yan *et al.* [16] by retraining their model using the default settings on our trainset. The results confirm that our approach consistently outperforms theirs in both photometric and motion measures as demonstrated in Table III.

D. Qualitative Comparison

Our method is evaluated against current methods on different benchmarks. We follow the settings used by Yan *et al.* [16] to compare with existing methods [6]–[8], [10], [74] in Fig. 5, and ours outperforms the others. In addition, due to limited open-source options, we compare with Yan *et al.* method

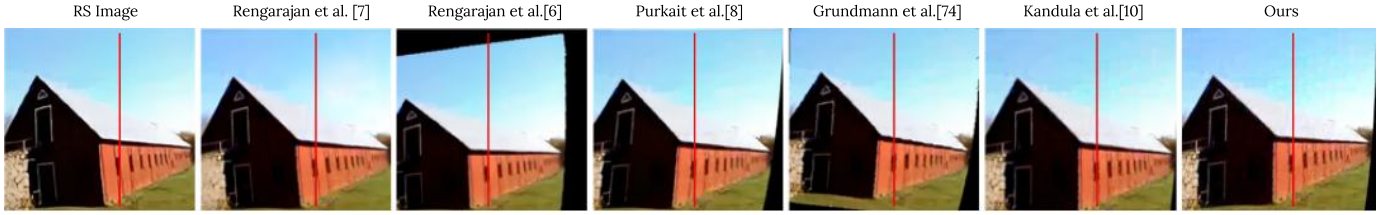


Fig. 5. Comparison with existing methods: Rengarajan *et al.* [7], Rengarajan *et al.* [6], Purkait *et al.* [8], Grundmann *et al.* [74] and Kandula *et al.* [10] on a RS building image. Red vertical lines to highlight correction results.

on the remaining datasets. We visualize RS and ground-truth GS images in the first two columns, then present Yan *et al.* results paired with alignment heatmaps that use darker shades to indicate greater similarity compared to GT images. We then display our own results alongside their corresponding alignment heatmaps, illustrating our approach’s consistency with benchmarks and precision in alignment. This visual comparison highlights the effectiveness of our methodology.

RS-Homo Dataset. We select seven representative examples from the dataset in Fig. 6. In the first three rows, we display RS images from a typical scenario characterized by rich textures and evident RS motion. In this case, our method consistently outperforms theirs. In the fourth row, we present an RS image captured in a scene with moving objects. Our method demonstrates its capability to handle such challenging conditions, delivering superior results as evidenced by the RS-corrected images and their alignment heatmaps. In the fifth to seventh rows, we present examples from low-texture scenes and nighttime scenes. Notably, our method excels at producing accurate corrections, in contrast to the comparison method, which tends to over-correct the RS image.

RS-Real Dataset. The new benchmark comprises more challenging RS images and varied RS motions as shown in Fig. 7. The first four rows compare performances for different RS directions; right-skewed and left-skewed. Our method outperforms Yan *et al.* [16], proving its effectiveness. The fifth and sixth rows feature RS images from quick device movement that produces intricate motion patterns, such as curved buildings. Our method effectively corrects the RS motion while the comparison method fails. The final three rows present complex scenarios with moving cars; the comparative method struggles with this complexity, resulting in incomplete corrections, whereas our framework efficiently manages these dynamic elements. This selection highlights our approach’s robustness across diverse and realistic RS challenges.

E. Experiment of testing on global shutter images

In previous experiments, our model was trained on RS-IGF-GS pairs, thus naturally performing well in converting images from rolling shutter to global shutter. Additionally, we are curious about the performance of the trained model when given global shutter images as input. Therefore, we conducted experiments, the results of which are presented in the second row of Table IV and the second column of Fig. 8. Although the experimental results demonstrate that our model does not

easily handle GS images, we believe the main reason lies in the absence of global shutter images during training.

To address this issue, we randomly sample 20% of the training data, utilizing the GS frames. The corresponding intra-gyro-fields are set to be all-zero, and we fine-tune our model for an additional 50,000 steps. More specifically, we crop 300×400 patches from the 600×800 GS images. The experimental results indicate that, after fine-tuning, our model gains the ability to handle global shutter inputs effectively, as illustrated in the last column of Fig. 8 and the third row of Table IV. Furthermore, the ability of the model to correct RS frames is further enhanced.

F. Generalizability Experiments

Experiments involve capturing new RS images with a “ONEPLUS 11” smartphone. These images are subsequently subjected to zero-shot inference using a model that has been pre-trained on the **RS-Real** dataset. It is important to note that the **RS-Real** dataset comprises images captured using a “XIAOMI CC9Pro” smartphone. The outcomes of these experiments are illustrated in Fig. 9.

Despite the fact that RS artifacts often correlate with specific sensors and devices, our framework’s robust backbone architecture ensures its generalizability across different mobile devices. This generalizability is critical for practical applications, as it demonstrates that the model can effectively handle RS images captured from a variety of devices without significant loss of performance. This capability is particularly valuable in real-world scenarios where the diversity of capturing devices can pose a significant challenge. By leveraging the robust features learned from the **RS-Real** dataset, our model can maintain high accuracy and reliability, regardless of the source device used for image capture.

G. Ablation Studies

We evaluate our framework design through experiments, starting with comparisons under diverse generative objectives, paired with analytical analyses. The effectiveness of the Patch-Attention Block is then scrutinized. Lastly, we explore the trade-off between performance and resolution.

1) *Predicting IGF vs. GS Image:* We contrast our “image-to-motion” pipeline with traditional “image-to-image” methods that use diffusion models to convert RS images to GS images at a fixed resolution of 256×256 , later upscaled to 600×800 for visual metric comparison with GT GS images,

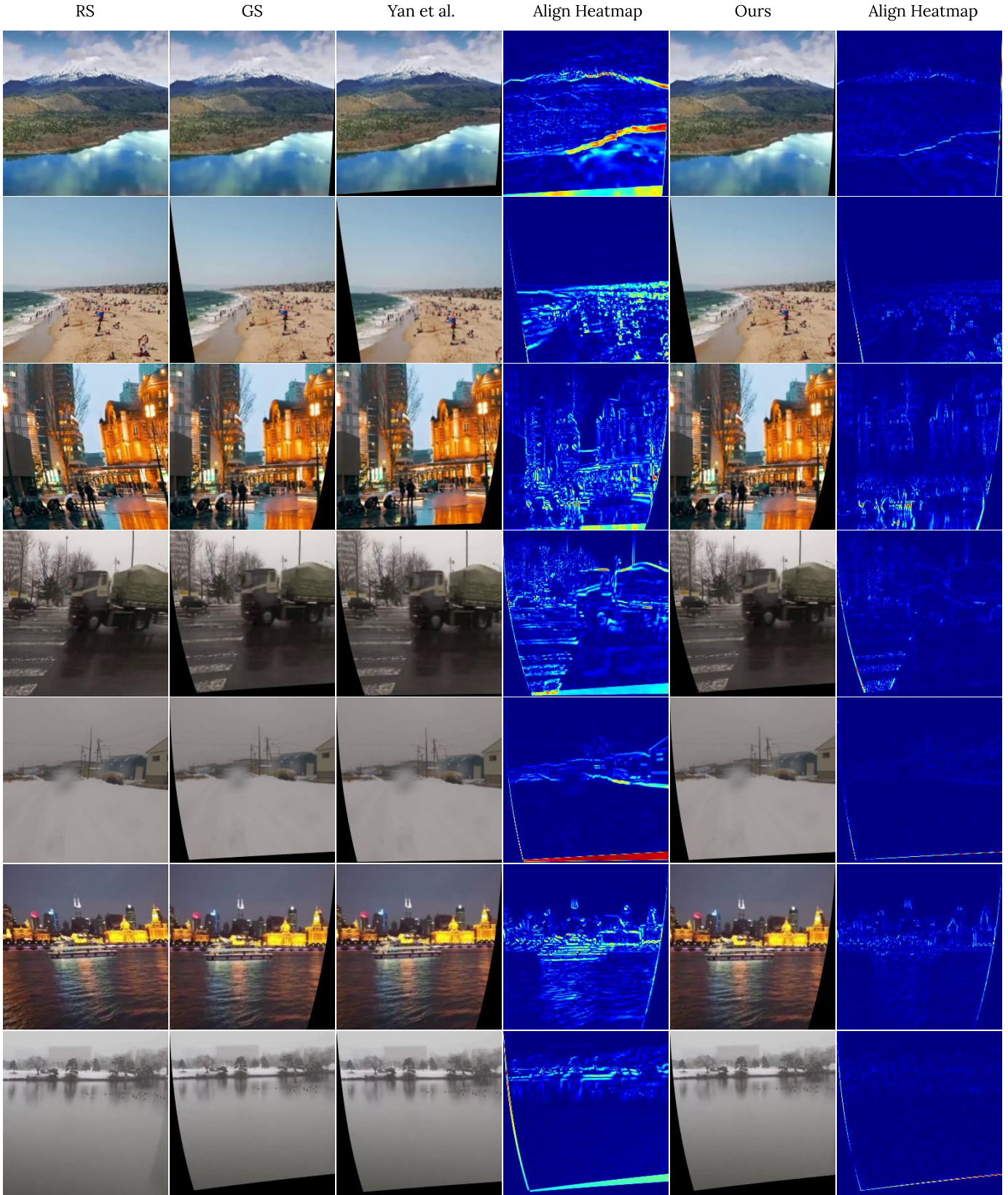


Fig. 6. Comparison on **RS-Homo** dataset. Column 1 shows the input RS image and Column 2 shows the ground-truth GS image. Column 3 and 5 are results by Yan *et al.* [16] and our method with the alignment heatmaps that use darker shades to indicate greater similarity compared to ground-truth GS images.

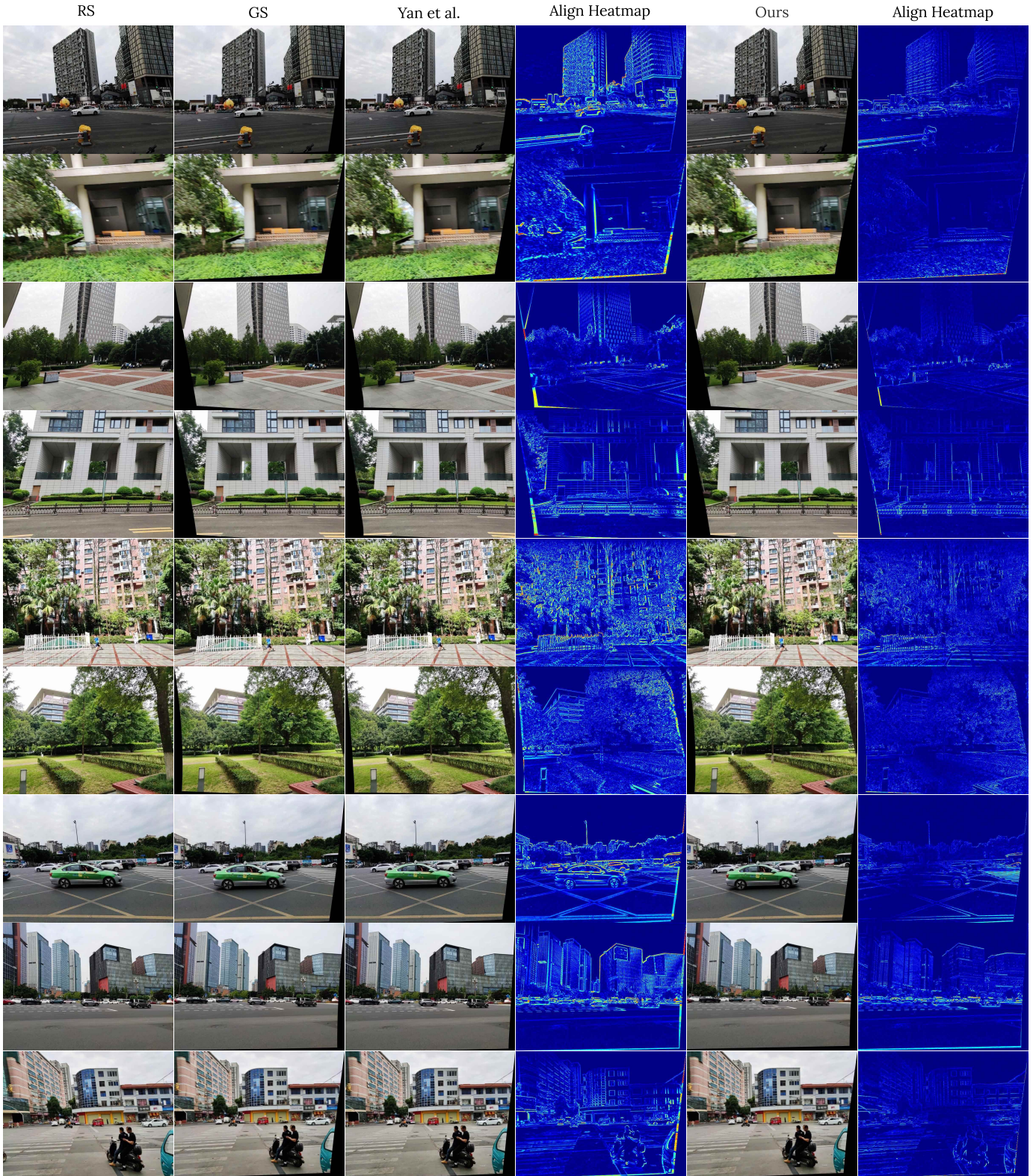


Fig. 7. Comparison on **RS-Real** dataset. Column 1 shows the input RS image and Column 2 shows the ground-truth GS image. Column 3 and 5 are results by Yan *et al.* [16] and our method with the alignment heatmaps that use darker shades to indicate greater similarity compared to ground-truth GS images.

TABLE IV

COMPARISON OF PSNR, SSIM, AND EPE BETWEEN OUR MODEL BEFORE FINE-TUNING AND AFTER FINE-TUNING ON THE **RS-REAL** DATASET. THE INPUT DATA TYPES INCLUDE ROLLING SHUTTER AND GLOBAL SHUTTER. THE VALUES ENCLOSED WITHIN PARENTHESES INDICATE THE STANDARD DEVIATION OF OUR RESULTS OVER 10 INFERENCE ITERATIONS.

Model	Input data	PSNR(dB) \uparrow	SSIM \uparrow	EPE \downarrow
Before Fine-tuning	RS	22.02(\pm 0.031)	0.70(\pm 0.001)	2.12(\pm 0.010)
	GS	16.78(\pm 0.528)	0.47(\pm 0.532)	7.56(\pm 0.425)
After Fine-tuning	RS	22.25 (\pm 0.023)	0.71 (\pm 0.001)	2.06 (\pm 0.017)
	GS	38.65 (\pm 0.025)	0.98 (\pm 0.031)	0.097 (\pm 0.005)

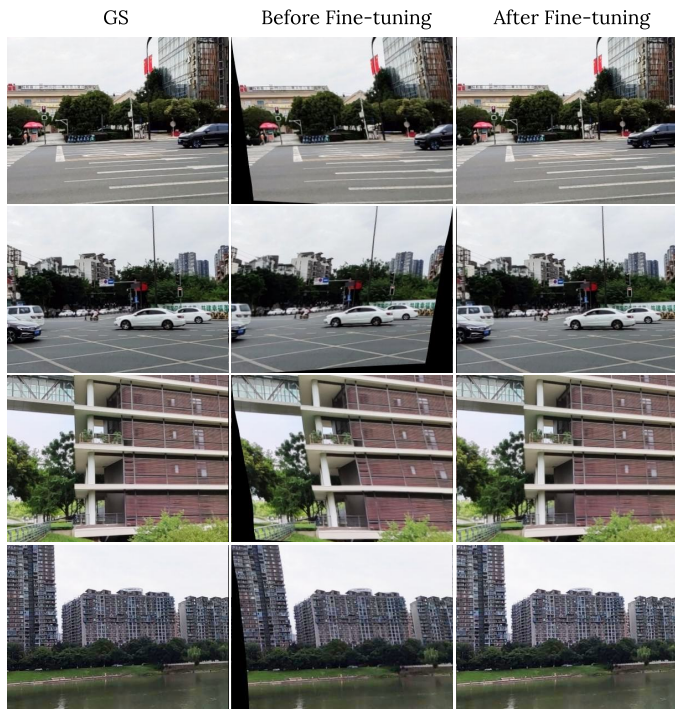


Fig. 8. Comparison illustration of global shutter inputs before and after fine-tuning. The first row represents the input global shutter images, the second row depicts the correction effect before model fine-tuning, and the third row shows the correction effect after model fine-tuning.

as shown in Table. V. Our approach significantly outperforms the conventional framework in the RS removal task for two main reasons: 1) It is not constrained by diffusion model resolutions, since we can upsample IGF to correct RS images at their original size; 2) While “image-to-image” models learn the joint probability distribution between RS and GS images, our method gains additional improvements by learning from the distribution involving RS images, GS images, and IGFs, thus leveraging more information for enhanced results.

TABLE V

COMPARISON BETWEEN DIFFERENT GENERATING OBJECTS.

“IMAGE-TO-IMAGE” INDICATES TRANSFORMING RS IMAGES TO GS ONES. “IMAGE-TO-MOTION” REPRESENTS PREDICTING IGFs FROM RS IMAGES.

Method	PSNR(dB) \uparrow	SSIM \uparrow
“image-to-image”	16.73	0.47
“image-to-motion”	20.78	0.63

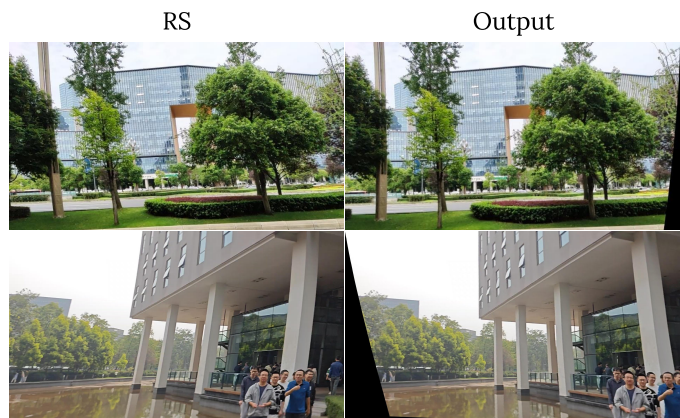


Fig. 9. The illustration of results that we leverage the pre-trained model on **RS-Real** to zero-shot inference on newly captured RS images using other mobile devices.

2) *Rolling-Shutter Patch Attention*: As illustrated in Table. VI, our proposed Patch Attention module is effective as it not only aggregates features within patches, but also interacts with features between patches. The experimental results are also consistent with our a priori knowledge of RS motion.

TABLE VI

THE EFFECTIVENESS OF PATCH ATTENTION. INTRA REFERS TO INTRA-PATCH ATTENTION AND INTER INDICATES INTER-PATCH ATTENTION.

Intra	Inter	PSNR(dB) \uparrow	SSIM \uparrow	EPE \downarrow
		20.78	0.63	2.62
✓		21.10	0.65	2.54
✓	✓	22.02	0.70	2.12

3) *Different Resolutions*: Experimenting with different resolutions, our findings are summarized in Table. VII. Notably, the benefit of higher resolution plateaus at 64, with any further increase leading to a decrease in results. This can be attributed to the global nature of RS motion, which only necessitates sufficient resolution rather than very high definition.

TABLE VII

COMPARISON BETWEEN DATA RESOLUTION AND PERFORMANCE.

Resolution	PSNR(dB) \uparrow	SSIM \uparrow	EPE \downarrow
32	21.30	0.66	2.37
64	22.02	0.70	2.12
128	21.37	0.66	2.36

V. LIMITATION

In the proposed **RS-Real dataset**, rolling shutter effects primarily result from camera rotation, though many instances also stem from camera translation and moving objects. Since the gyroscope records only the camera’s rotation, our dataset concentrates on rotation-induced RS images. It neglects the rolling shutter effects and corresponding correction flows caused by camera translation and moving objects, representing this work’s major limitation. Despite these limitations in our dataset and model, we believe that our dataset still provides an effective benchmark for the single-frame rolling shutter correction task, capable of advancing the field.

VI. CONCLUSION

In this work, we have presented RS-Diffusion, the first Diffusion Model based approach for single frame rolling shutter rectification. We have captured a novel dataset, namely RS-Real, specifically tailored for this task. The RS-Real dataset contains captured RS images, and the corresponding ground-truth GS images can be created according to synchronized gyroscope data that recorded during the RS frame capturing, yielding RS-GS image pairs. Uniquely, this dataset fulfills both accuracy and authenticity requirements for RS research. In addition, we have presented the first diffusion models based framework for real-time RS correction using just one RS frame. We have achieved state-of-the-art performances when compared to previous single RS correction methods. To facilitate further research, we will publicly share our code and dataset with the community.

REFERENCES

- [1] J. Hedborg, P.-E. Forssén, M. Felsberg, and E. Ringaby, “Rolling shutter bundle adjustment,” in *Proc. CVPR*, 2012, pp. 1434–1441.
- [2] O. Saurer, M. Pollefeys, and G. H. Lee, “Sparse to dense 3D reconstruction from rolling shutter images,” in *Proc. CVPR*, 2016, pp. 3337–3345.
- [3] C. Albl, Z. Kukulova, and T. Pajdla, “R6P-rolling shutter absolute camera pose,” in *Proc. CVPR*, 2015, pp. 2292–2300.
- [4] O. Saurer, K. Koser, J.-Y. Bouquet, and M. Pollefeys, “Rolling shutter stereo,” in *Proc. ICCV*, 2013, pp. 465–472.
- [5] S. Liu, B. Xu, C. Deng, S. Zhu, B. Zeng, and M. Gabbouj, “A hybrid approach for near-range video stabilization,” *IEEE Transactions on Circuits and Systems for Video Technology*, vol. 27, no. 9, pp. 1922–1933, 2017.
- [6] V. Rengarajan, A. N. Rajagopalan, and R. Aravind, “From bows to arrows: Rolling shutter rectification of urban scenes,” in *Proc. CVPR*, 2016, pp. 2773–2781.
- [7] V. Rengarajan, Y. Balaji, and A. Rajagopalan, “Unrolling the shutter: CNN to correct motion distortions,” in *Proc. CVPR*, 2017, pp. 2291–2299.
- [8] P. Purkait, C. Zach, and A. Leonardis, “Rolling shutter correction in manhattan world,” in *Proc. ICCV*, 2017, pp. 882–890.
- [9] B. Zhuang, Q.-H. Tran, P. Ji, L.-F. Cheong, and M. Chandraker, “Learning structure-and-motion-aware rolling shutter correction,” in *Proc. CVPR*, 2019, pp. 4551–4560.
- [10] P. Kandula, T. L. Kumar, and A. Rajagopalan, “Deep end-to-end rolling shutter rectification,” *JOSA A*, vol. 37, no. 10, pp. 1574–1582, 2020.
- [11] C.-K. Liang, L.-W. Chang, and H. H. Chen, “Analysis and compensation of rolling shutter effect,” *IEEE Trans. Image Process.*, vol. 17, no. 8, pp. 1323–1330, 2008.
- [12] E. Ringaby and P.-E. Forssén, “Efficient video rectification and stabilisation for cell-phones,” *International Journal of Computer Vision(IJCV)*, vol. 96, no. 3, pp. 335–352, 2012.
- [13] B. Zhuang, L.-F. Cheong, and G. Hee Lee, “Rolling-shutter-aware differential SFM and image rectification,” in *Proc. ICCV*, 2017, pp. 948–956.
- [14] S. Vasu, A. Rajagopalan *et al.*, “Occlusion-aware rolling shutter rectification of 3d scenes,” in *Proc. CVPR*, 2018, pp. 636–645.
- [15] Y.-G. Kim, V. R. Jayanthi, and I.-S. Kweon, “System-on-chip solution of video stabilization for cmos image sensors in hand-held devices,” *IEEE Trans. Circuits and Systems for Video Technology*, vol. 21, no. 10, pp. 1401–1414, 2011.
- [16] W. Yan, R. T. Tan, B. Zeng, and S. Liu, “Deep homography mixture for single image rolling shutter correction,” in *Proc. ICCV*, 2023, pp. 9868–9877.
- [17] T. Brown, B. Mann, N. Ryder, M. Subbiah, J. D. Kaplan, P. Dhariwal, A. Neelakantan, P. Shyam, G. Sastry, A. Askell *et al.*, “Language models are few-shot learners,” *Proc. NeurIPS*, vol. 33, pp. 1877–1901, 2020.
- [18] I. Goodfellow, J. Pouget-Abadie, M. Mirza, B. Xu, D. Warde-Farley, S. Ozair, A. Courville, and Y. Bengio, “Generative adversarial networks,” *Communications of the ACM*, vol. 63, no. 11, pp. 139–144, 2020.
- [19] L. Ouyang, J. Wu, X. Jiang, D. Almeida, C. Wainwright, P. Mishkin, C. Zhang, S. Agarwal, K. Slama, A. Ray *et al.*, “Training language models to follow instructions with human feedback,” *Proc. NeurIPS*, vol. 35, pp. 27730–27744, 2022.
- [20] J. Ho, A. Jain, and P. Abbeel, “Denosing diffusion probabilistic models,” in *Proc. NeurIPS*, 2020, pp. 6840–6851.
- [21] Y. Song, J. Sohl-Dickstein, D. P. Kingma, A. Kumar, S. Ermon, and B. Poole, “Score-based generative modeling through stochastic differential equations,” *arXiv preprint arXiv:2011.13456*, 2020.
- [22] G. Tevet, S. Raab, B. Gordon, Y. Shafir, D. Cohen-Or, and A. H. Bermato, “Human motion diffusion model,” *arXiv preprint arXiv:2209.14916*, 2022.
- [23] S. Saxena, C. Herrmann, J. Hur, A. Kar, M. Norouzi, D. Sun, and D. J. Fleet, “The surprising effectiveness of diffusion models for optical flow and monocular depth estimation,” *arXiv preprint arXiv:2306.01923*, 2023.
- [24] S. Gao, X. Liu, B. Zeng, S. Xu, Y. Li, X. Luo, J. Liu, X. Zhen, and B. Zhang, “Implicit diffusion models for continuous super-resolution,” in *Proc. CVPR*, 2023, pp. 10021–10030.
- [25] W. Yinhuai, Y. Jiwen, and Z. Jian, “Zero-shot image restoration using denoising diffusion null-space model,” *arXiv preprint arXiv:2212.00490*, 2022.
- [26] Q. Yan, T. Hu, Y. Sun, H. Tang, Y. Zhu, W. Dong, L. Van Gool, and Y. Zhang, “Toward high-quality hdr deghosting with conditional diffusion models,” *IEEE Trans. Circuits and Systems for Video Technology*, vol. 34, no. 5, pp. 4011–4026, 2024.
- [27] Z. Yang, T. Chu, X. Lin, E. Gao, D. Liu, J. Yang, and C. Wang, “Eliminating contextual prior bias for semantic image editing via dual-cycle diffusion,” *IEEE Trans. Circuits and Systems for Video Technology*, vol. 34, no. 2, pp. 1316–1320, 2024.
- [28] J. Ho and T. Salimans, “Classifier-free diffusion guidance,” *arXiv preprint arXiv:2207.12598*, 2022.
- [29] J. Song, C. Meng, and S. Ermon, “Denosing diffusion implicit models,” *arXiv preprint arXiv:2010.02502*, 2020.
- [30] Y. Han, K. Luo, A. Luo, J. Liu, H. Fan, G. Luo, and S. Liu, “RealFlow: EM-based realistic optical flow dataset generation from videos,” in *Proc. ECCV*, 2022, pp. 288–305.
- [31] S. Baker, E. Bennett, S. B. Kang, and R. Szeliski, “Removing rolling shutter wobble,” in *Proc. CVPR*, 2010, pp. 2392–2399.
- [32] P. Liu, Z. Cui, V. Larsson, and M. Pollefeys, “Deep shutter unrolling network,” in *Proc. CVPR*, 2020, pp. 5941–5949.
- [33] B. Fan, Y. Dai, and M. He, “SUNet: symmetric undistortion network for rolling shutter correction,” in *Proc. CVPR*, 2021, pp. 4541–4550.
- [34] M. Cao, Z. Zhong, J. Wang, Y. Zheng, and Y. Yang, “Learning adaptive warping for real-world rolling shutter correction,” in *Proc. CVPR*, 2022, pp. 17785–17793.
- [35] B. Fan, Y. Mao, Y. Dai, Z. Wan, and Q. Liu, “Joint appearance and motion learning for efficient rolling shutter correction,” in *Proc. CVPR*, 2023, pp. 5671–5681.
- [36] B. Fan, Y. Dai, and H. Li, “Learning bilateral cost volume for rolling shutter temporal super-resolution,” *IEEE Trans. Pattern Anal. Mach. Intell.*, 2024.
- [37] Z. Zhong, Y. Zheng, and I. Sato, “Towards rolling shutter correction and deblurring in dynamic scenes,” in *Proc. CVPR*, 2021, pp. 9219–9228.
- [38] C. Albl, Z. Kukulova, V. Larsson, M. Polic, T. Pajdla, and K. Schindler, “From two rolling shutters to one global shutter,” in *Proc. CVPR*, 2020, pp. 2505–2513.
- [39] Z. Zhong, M. Cao, X. Sun, Z. Wu, Z. Zhou, Y. Zheng, S. Lin, and I. Sato, “Bringing rolling shutter images alive with dual reversed distortion,” in *Proc. ECCV*, 2022, pp. 233–249.

- [40] W. Shang, D. Ren, C. Feng, X. Wang, L. Lei, and W. Zuo, "Self-supervised learning to bring dual reversed rolling shutter images alive," in *Proc. ICCV*, 2023, pp. 13 086–13 094.
- [41] Y. Lao and O. Ait-Aider, "A robust method for strong rolling shutter effects correction using lines with automatic feature selection," in *Proc. CVPR*, 2018, pp. 4795–4803.
- [42] J. Sohl-Dickstein, E. Weiss, N. Maheswaranathan, and S. Ganguli, "Deep unsupervised learning using nonequilibrium thermodynamics," in *Proc. ICML*, 2015, pp. 2256–2265.
- [43] Y. Song and S. Ermon, "Generative modeling by estimating gradients of the data distribution," in *Proc. NeurIPS*, 2019, pp. 1–9.
- [44] P. Dhariwal and A. Nichol, "Diffusion models beat GANs on image synthesis," in *Proc. NeurIPS*, 2021, pp. 8780–8794.
- [45] X. Liu, D. H. Park, S. Azadi, G. Zhang, A. Chopikyan, Y. Hu, H. Shi, A. Rohrbach, and T. Darrell, "More control for free! image synthesis with semantic diffusion guidance," in *Proc. WACV*, 2023, pp. 289–299.
- [46] R. Rombach, A. Blattmann, D. Lorenz, P. Esser, and B. Ommer, "High-resolution image synthesis with latent diffusion models," in *Proc. CVPR*, 2022, pp. 10 684–10 695.
- [47] Y. Wang, J. Yu, and J. Zhang, "Zero-shot image restoration using denoising diffusion null-space model," *arXiv preprint arXiv:2212.00490*, 2022.
- [48] H. Ni, C. Shi, K. Li, S. X. Huang, and M. R. Min, "Conditional image-to-video generation with latent flow diffusion models," in *Proc. CVPR*, 2023, pp. 18 444–18 455.
- [49] T. Zhou, H. Li, Z. Wang, A. Luo, C.-L. Zhang, J. Li, B. Zeng, and S. Liu, "Recdiffusion: Rectangling for image stitching with diffusion models," *arXiv preprint arXiv:2403.19164*, 2024.
- [50] H. Xu, H. Li, Y. Wang, S. Liu, and C.-W. Fu, "Handbooster: Boosting 3d hand-mesh reconstruction by conditional synthesis and sampling of hand-object interactions," *arXiv preprint arXiv:2403.18575*, 2024.
- [51] H. Li, H. Jiang, A. Luo, P. Tan, H. Fan, B. Zeng, and S. Liu, "Dm homo: Learning homography with diffusion models," *ACM Transactions on Graphics*, vol. 43, no. 3, pp. 1–16, 2024.
- [52] A. Karpenko, D. Jacobs, J. Baek, and M. Levoy, "Digital video stabilization and rolling shutter correction using gyroscopes," *Computer and Structures*, vol. 1, no. 2, p. 13, 2011.
- [53] S. Bell, A. Troccoli, and K. Pulli, "A non-linear filter for gyroscope-based video stabilization," in *Proc. ECCV*, 2014, pp. 294–308.
- [54] J. Mustaniemi, J. Kannala, S. Särkkä, J. Matas, and J. Heikkilä, "Gyroscope-aided motion deblurring with deep networks," in *Proc. WACV*, 2019, pp. 1914–1922.
- [55] K. Zhang, W. Ren, W. Luo, W.-S. Lai, B. Stenger, M.-H. Yang, and H. Li, "Deep image deblurring: A survey," *International Journal of Computer Vision*, vol. 130, no. 9, pp. 2103–2130, 2022.
- [56] S. Liu, H. Li, Z. Wang, J. Wang, S. Zhu, and B. Zeng, "DeepOIS: Gyroscope-guided deep optical image stabilizer compensation," *IEEE Trans. Circuits and Systems for Video Technology*, vol. 32, no. 5, pp. 2856–2867, 2021.
- [57] W. Huang and H. Liu, "Online initialization and automatic camera-imu extrinsic calibration for monocular visual-inertial slam," in *Proc. ICRA*, 2018, pp. 5182–5189.
- [58] C.-R. Lee, J. H. Yoon, M.-G. Park, and K.-J. Yoon, "Gyroscope-aided relative pose estimation for rolling shutter cameras," *arXiv preprint arXiv:1904.06770*, 2019.
- [59] M. Bloesch, S. Omari, P. Fankhauser, H. Sommer, C. Gehring, J. Hwangbo, M. A. Hoepflinger, M. Hutter, and R. Siegwart, "Fusion of optical flow and inertial measurements for robust egomotion estimation," in *Proc. IROS*, 2014, pp. 3102–3107.
- [60] C. Malleon, J. Collomosse, and A. Hilton, "Real-time multi-person motion capture from multi-view video and imus," *International Journal of Computer Vision(IJCV)*, vol. 128, pp. 1594–1611, 2020.
- [61] A. Gilbert, M. Trumble, C. Malleon, A. Hilton, and J. Collomosse, "Fusing visual and inertial sensors with semantics for 3d human pose estimation," *International Journal of Computer Vision(IJCV)*, vol. 127, pp. 381–397, 2019.
- [62] J. Mo, M. J. Islam, and J. Sattar, "Imu-assisted learning of single-view rolling shutter correction," 2022, pp. 861–870.
- [63] C. Jia and B. L. Evans, "Online calibration and synchronization of cellphone camera and gyroscope," in *IEEE Global Conference on Signal and Information Processing*, 2013, pp. 731–734.
- [64] H. Li, K. Luo, B. Zeng, and S. Liu, "Gyroflow+: Gyroscope-guided unsupervised deep homography and optical flow learning," *International Journal of Computer Vision(IJCV)*, pp. 1–19, 2024.
- [65] J. S. Dai, "Euler–rodriques formula variations, quaternion conjugation and intrinsic connections," *Mechanism and Machine Theory*, vol. 92, pp. 144–152, 2015.
- [66] R. Hartley and A. Zisserman, *Multiple view geometry in computer vision*. Cambridge university press, 2003.
- [67] P.-E. Forssén and E. Ringaby, "Rectifying rolling shutter video from hand-held devices," in *Proc. CVPR*, 2010, pp. 507–514.
- [68] N. Joshi, S. B. Kang, C. L. Zitnick, and R. Szeliski, "Image deblurring using inertial measurement sensors," *ACM Transactions on Graphics (TOG)*, vol. 29, no. 4, pp. 1–9, 2010.
- [69] Y. Dai, H. Li, and L. Kneip, "Rolling shutter camera relative pose: Generalized epipolar geometry," in *Proc. CVPR*, 2016, pp. 4132–4140.
- [70] H. Li, K. Luo, and S. Liu, "GyroFlow: gyroscope-guided unsupervised optical flow learning," in *Proc. ICCV*, 2021, pp. 12 869–12 878.
- [71] J. Xiao, J. Hays, K. A. Ehinger, A. Oliva, and A. Torralba, "SUN database: Large-scale scene recognition from abbey to zoo," in *Proc. CVPR*, 2010, pp. 3485–3492.
- [72] H. Shao, T. Svoboda, and L. Van Gool, "Zubud-zurich buildings database for image based recognition," vol. 260, pp. 6–8, 2003.
- [73] J. Philbin, O. Chum, M. Isard, J. Sivic, and A. Zisserman, "Object retrieval with large vocabularies and fast spatial matching," in *Proc. CVPR*, 2007, pp. 1–8.
- [74] M. Grundmann, V. Kwatra, D. Castro, and I. Essa, "Calibration-free rolling shutter removal," in *Proc. ICCP*, 2012, pp. 1–8.